

# Structural Assessment of Advanced Composite Tow-Steered Shells

**K. Chauncey Wu<sup>1</sup>, Bret K. Stanford<sup>2</sup>, Glenn A. Hrinda<sup>3</sup>,  
Zhuosong Wang<sup>4</sup>, Robert A. Martin<sup>5</sup>**

*NASA Langley Research Center, Hampton, Virginia 23681*

and

**H. Alicia Kim<sup>6</sup>**

*University of Bath, Bath, United Kingdom*

**The structural performance of two advanced composite tow-steered shells, manufactured using a fiber placement system, is assessed using both experimental and analytical methods. The fiber orientation angles vary continuously around the shell circumference from  $\pm 10$  degrees on the shell crown and keel, to  $\pm 45$  degrees on the shell sides. The two shells differ in that one shell has the full 24-tow course applied during each pass of the fiber placement system, while the second shell uses the fiber placement system's tow drop/add capability to achieve a more uniform shell wall thickness. The shells are tested in axial compression, and estimates of their prebuckling axial stiffnesses and bifurcation buckling loads are predicted using linear finite element analyses. These preliminary predictions compare well with the test results, with an average agreement of approximately 10 percent.**

## I. Introduction

Strength and stiffness tailoring of conventional composite laminates has typically been accomplished by orienting variable numbers of unidirectional plies at a limited subset (typically 0,  $\pm 45$  and 90 degrees) of the potential fiber orientation angles. However, advanced composite tow-steered structures, where the fiber angle is allowed to vary continuously over the structural planform within each ply, have received increased interest because of their potential to further reduce weight and increase structural performance over conventional composites (Ref. 1). Although strength and stiffness tailoring of advanced composites may improve their structural performance, their design is more challenging due to the increased number of design variables (i.e., spatial variation of the fiber orientation angles).

These tow-steered structures can be readily fabricated using automated fiber placement systems (Figure 1; Ref. 2) that are widely used in the aerospace industry. These computer-numerically-controlled machines can laminate up to 32 continuous, unidirectional prepreg tows or slit-tape material, each 1/8 to 1/2 in.-wide, onto a mandrel or tool surface while precisely and accurately

---

<sup>1</sup> Senior Aerospace Engineer, Structural Mechanics and Concepts Branch, RD.

<sup>2</sup> Aerospace Engineer, Aeroelasticity Branch, RD. AIAA Member.

<sup>3</sup> Senior Aerospace Engineer, Vehicle Analysis Branch, SACD. AIAA Senior Member.

<sup>4</sup> LARSS Student, assigned to the Structural Mechanics and Concepts Branch, RD.

<sup>5</sup> Aerospace Engineer, Mechanical Systems Branch, ED.

<sup>6</sup> Senior Lecturer in Aerospace Structures, Mechanical Engineering Department. AIAA Senior Member.



Figure 1. Fiber placement system (Lockheed Martin)

following pre-defined curvilinear spatial paths, or courses. However, tow-steered structures have not been widely deployed in operational service, and so have not been tested as extensively as more conventional straight-fiber composites. In addition, the techniques required for their structural design, modeling, analyses and certification are not currently well defined or understood, as they are for more conventional composites.

To further expand the database of knowledge and experience with advanced composite structures, the structural performance of two prototype tow-steered shells (one of which is shown in Figure 2) is evaluated using both experimental and finite element methods, and the preliminary results are presented herein. Design trade studies of the performance of the present (and other) shell configurations are presented in Ref. 3, and their manufacture is described in Ref. 4. Concurrent work to assess several tow-steered, “variable stiffness” shells under both free vibration and transverse bending moments is documented by Blom, et al., in Refs. 5 and 6. Fabrication and testing of two conventional quasi-isotropic thermoplastic shells using similar manufacturing processes is also described in Ref. 7.



Figure 2. Advanced composite tow-steered shell

Both of the cylindrical shells investigated in this study have a nominal 8-ply laminate thickness, and fiber orientation angles that vary continuously around the cylinder circumference. These shells are designed to have different cross-sectional bending stiffnesses about their transverse

axes, as described in Ref. 3. One possible application for this type of structure could be in an advanced commercial aircraft fuselage under applied flight loads, which may behave like a beam in bending where the crown and keel experience compression and tension loads, and the shell sides are subjected to shear. For this study, the experimental studies and finite element analyses are conducted under axial compression loads, and the buckling and post-buckling behaviors of these cylinders are evaluated herein.

## II. Tow-steered shells description

Two prototype advanced composite tow-steered shells are fabricated using a fiber placement system, as described in Ref. 4. The nominal inner diameter of both shells is 16.266 inches with an overall length of 35.0 inches. The shells are manufactured using 1/8 in.-wide IM7/8552 graphite/epoxy slit tape material oriented in a nominal 8-ply,  $[\pm 45/\pm \Theta]_s$  layup, where the fiber orientation angle  $\Theta$  varies continuously from  $\pm 10$  degrees on the shell crown and keel, to  $\pm 45$  degrees on the shell sides along a constant-radius circular arc (Ref. 3). Up to 24 tows are placed at any instant by the fiber placement system during fabrication of these shells.

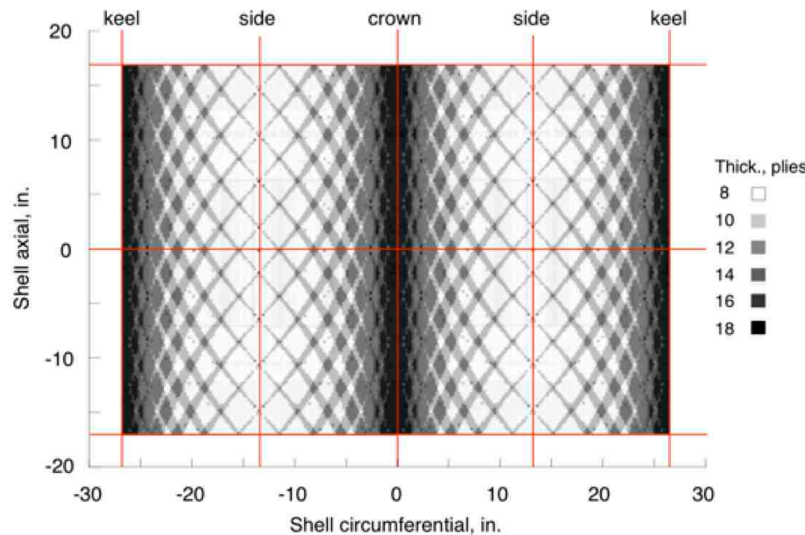


Figure 3. Predicted Shell A laminate thickness (Ref. 3)

When all of the available tows are placed during a given course, overlaps will appear between tows placed during adjacent courses, resulting in significant laminate thickness build-ups over the shell crown and keel regions (indicated by the shaded regions in Figure 3). The first shell evaluated in this study has these raised surface features, and is therefore designated as the shell with overlaps, or Shell A. Alternatively, individual tows may also be cut (or “dropped”) or added at any time during shell fabrication. This practice leads to more a uniform laminate thickness, but also creates small resin-rich pockets distributed over the shell planform at the tow drop locations (Figure 4). The second shell is fabricated using this tow drop/add capability, and is designated as the shell without overlaps, or Shell B.

The effective axial stiffness  $E_{eff}$  of an 8-ply  $[\pm 45/\pm \Theta]_s$  layup is calculated using classical lamination theory and the nominal IM7/8552 ply material properties (Ref. 8) listed in Table 1.

This effective stiffness is plotted for  $\Theta$  between 0 and 90 degrees in Figure 5. The data in the shaded region of this plot indicates that the relative crown/keel-to-side axial stiffness for Shell B varies by up to a factor of 2 over the range between 10 and 45 degrees. However, the larger number of  $\pm 10$  degree plies placed over the crown and keel regions of Shell A will increase the corresponding axial stiffness ratio for this shell.

Table 1. Nominal and measured IM7/8552 compressive ply properties

	$E_1$ , Mlb/in <sup>2</sup>	$E_2$ , Mlb/in <sup>2</sup>	$\nu_{12}$	$G_{12}$ , Mlb/in <sup>2</sup>
Nominal	20.44	1.41	0.356	0.68
Measured	18.04	1.26	0.347	0.70
Coeff. of variation, pct.	1.0	1.7	1.8	3.2

Cured ply thickness = 0.0054 in./ply, material density = 0.058 lb/in<sup>3</sup>

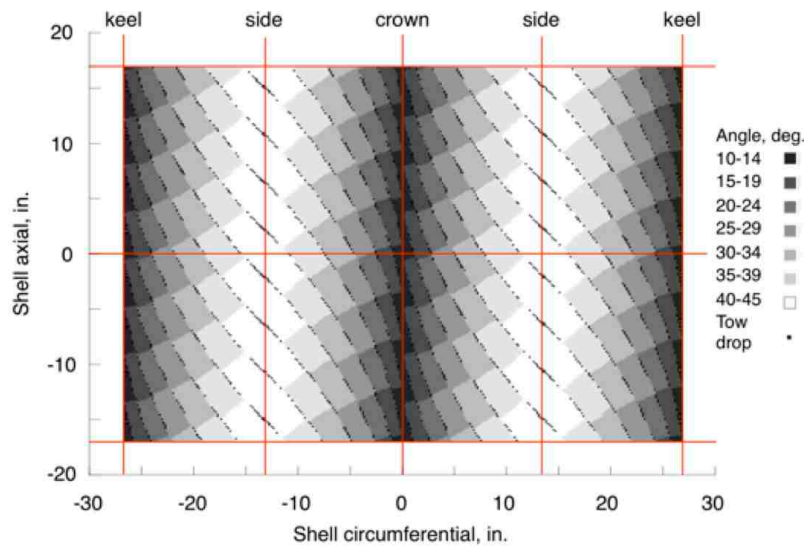


Figure 4. Predicted Shell B ply 3 fiber orientation angles and tow drops (Ref. 3)

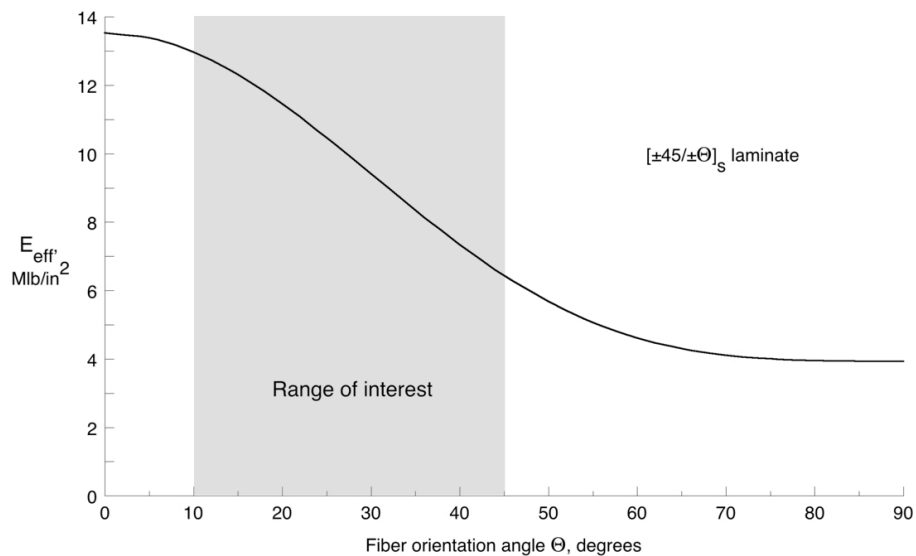


Figure 5.  $[\pm 45/\pm \Theta]_s$  laminate effective axial stiffness

### III. Material properties determination

As-manufactured compressive material properties are determined from two small witness panels that are fabricated using the same materials and processes as the tow-steered shells. The IM7/8552 material used has a nominal fiber areal weight of  $0.00020 \text{ lb/in}^2$  ( $145 \text{ g/m}^2$ ) and a 66 percent fiber volume fraction. These panels, with unidirectional  $[0]_{16}$  and cross-ply  $[0/90]_{4s}$  layups, are twice as thick as the nominal shell walls. Small coupons are cut from these panels at four different orientations ( $[0]_{16}$ ,  $[90]_{16}$ ,  $[0/90]_{4s}$  and  $[\pm 45]_{4s}$  layups) for the material characterization tests (Ref. 9). The laminate thicknesses of these specimens are also measured to determine the average 0.0054-in. ply thickness listed in Table 1. Biaxial strain gage rosettes are applied to both sides of the coupons at their centers, and used to measure the axial and transverse strains applied during the tests. The compressive forces on the coupons are also recorded during the tests, and are divided by their associated cross-sectional areas to obtain stresses. These measured stresses are then plotted against the corresponding strain data (e.g., Figure 6), and the linear slopes from these graphs are calculated and used to estimate the measured composite ply properties reported in Table 1.

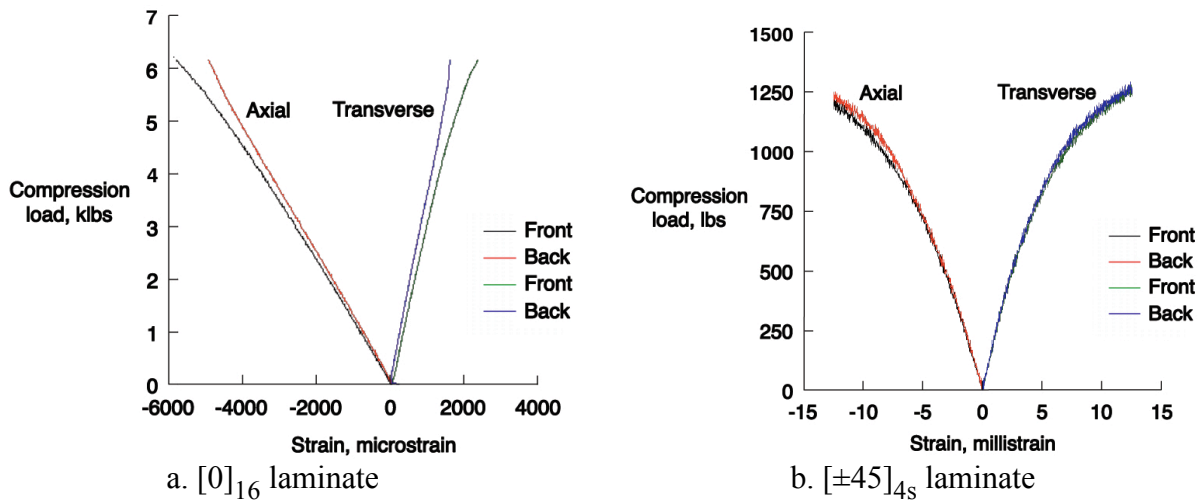


Figure 6. Representative coupon compression test data

The corresponding coefficients of variation (standard deviation divided by mean value) reported in Table 1 for the measured composite ply properties are all small, indicating that the test data are good. However, when compared with the nominal properties from Ref. 8, the measured material properties from the coupon tests are consistently lower. The poorest correlation is noted for the measured ply moduli  $E_1$  and  $E_2$ , which are both about 11 percent lower than their nominal values. The reduction in  $E_1$  may be due to the presence of discontinuous fibers in the slit tape (cut or broken in the slitting process) used during manufacture of the shells and panels. In comparison, the coupons fabricated to determine the nominal material properties are manufactured using hand layup and unidirectional sheet material, which would contain much smaller numbers of cut fibers. Small differences are observed in the shear moduli  $G_{12}$ , which tends to be driven by the resin stiffness. However, this does not explain the corresponding reduction in  $E_2$ , which should also be a matrix-dominated property.

## IV. Shell axial compression tests

Axial compression tests, performed on the tow-steered shells to experimentally determine their nonlinear and buckling structural response, are described in this section. An overview of preparations for the shell tests and test set-up are given, followed by a discussion and interpretation of the test results.

### A. Test preparation

To prepare the composite shells for testing, they are first cut to their 35-in. finished lengths. The shells are then weighed, with Shell A (with overlaps) weighing 5.23 lbs, and Shell B (without overlaps) weighing 4.13 lbs. An epoxy resin potting compound is cast to a 1-in. depth around both ends of each shell (Figure 7) to prevent localized brooming failures of the shell ends. Thin, concentric aluminum rings are used to contain the potting while it cures, and are then left in place during the tests. The potted shell ends are then machined flat and parallel to ensure uniform contact with the test machine platens for uniform load introduction.



Figure 7. Potted end of tow-steered shell

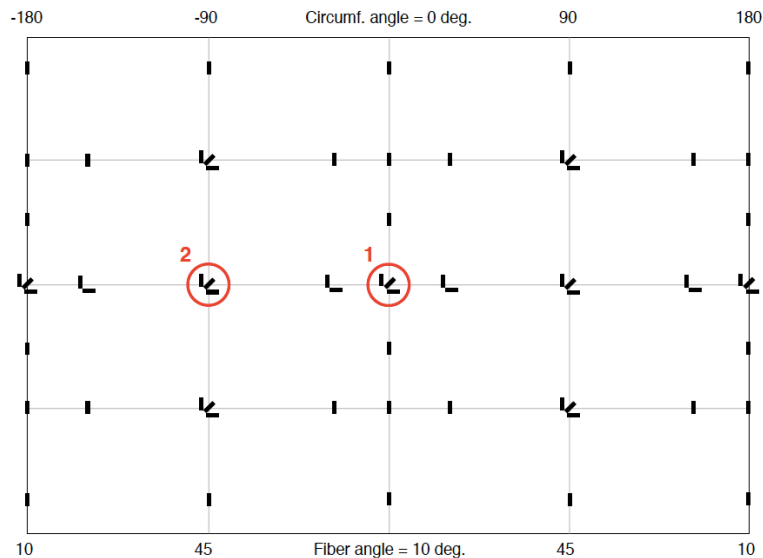


Figure 8. Strain gage locations

The shell geometric imperfections with the installed end fixtures are also measured using non-contacting laser metrology techniques. While the laminate thicknesses should still be identical to those reported in Ref. 4, machining the shells to length and potting the ends could have altered their geometric imperfections from their previous, unfixtured, values.

Prior to testing, a total of 56 back-to-back strain gage pairs are affixed to the shell outer and inner surfaces of both shells to measure the local strain responses over the shell planforms. Uniaxial, biaxial and triaxial strain gage rosettes are installed at the locations shown in Figure 8. The gages are concentrated around the shell crown and keel regions, and also along the shell sides, to thoroughly quantify the shell strain response to the applied loading.

## **B. Experimental set-up**

Structural tests are then performed on the two tow-steered shells to evaluate their response to applied quasi-static axial compression. A preliminary low-load test is first performed on each shell to verify performance of the data acquisition system. A final test to failure is then performed on each shell, and results from these latter tests are presented and discussed in this section. The tests are all performed in a displacement-control mode at a rate of approximately 1 klb/minute.

The experimental setup is shown in Figure 9, with a 300 klb-capacity electrohydraulic test machine used to apply controlled axial displacements to the shell ends. Data from the test machine's internal axial load cell and axial displacement readout are sent to an automated data acquisition system, along with measurements from the additional test instrumentation affixed to the shells. A thick, machined steel ring with small radial cutouts is centered on the lower platen of the test stand, and allows the strain gage wires from the shell interior to be brought outside of the shell and connected to the data acquisition system.

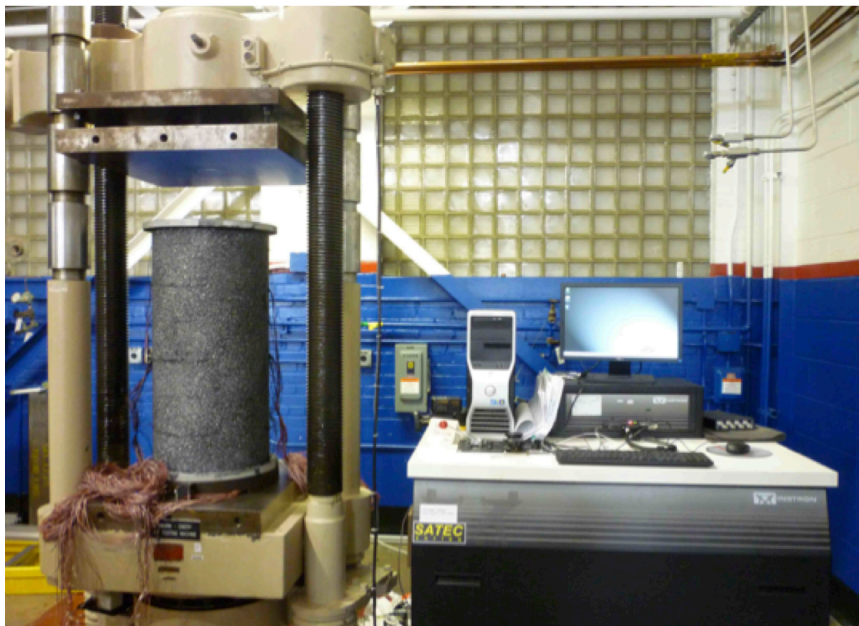


Figure 9. Experimental setup

Linear variable displacement transducers (LVDTs) are installed between each corner of the test stand's load platens to measure their relative displacement, and are used to assess the shells' axial displacement response to the applied end shortening. These individual measurements are first adjusted to pass through zero force at zero displacement, and are then averaged to determine the overall end shortening applied to the shell during the test.

### C. Test results - End shortening

These overall load-end shortening responses from the shell tests are plotted in Figure 10 for Shell A and Figure 11 for Shell B, and may both be divided into four distinct zones numbered 1 through 4. These zones, in increasing numerical order, broadly represent prebuckling, postbuckling, unloading, and elastic recovery, and each are discussed in more detail below.

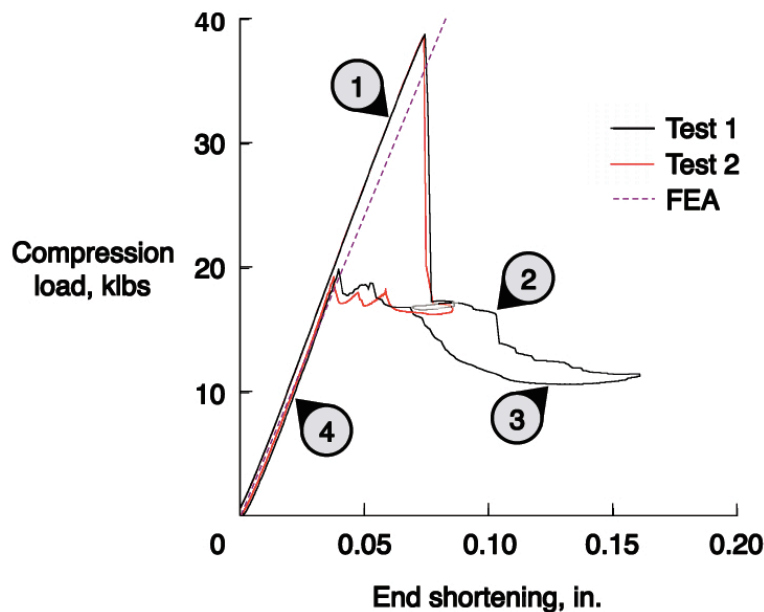


Figure 10. Shell A load-displacement plots

As shown in the figures, the prebuckling load-end shortening responses in Zone 1 are generally linear, with some minor nonlinearity at low loads and near buckling. The linear least-squares best-fit slopes of the load-end shortening curves in Figures 10 and 11 are calculated and reported below in Table 2. To avoid the effects of the slightly nonlinear shell responses at low loads (typically associated with deadband in the test machine) and near buckling, these prebuckling axial stiffnesses are estimated between 2.5 and 30 klbs for Shell A, and 2 and 15 klbs for Shell B. The calculated axial stiffness of Shell A is 62 percent higher than that of Shell B, which arises primarily from the additional stiffness of the overlapped  $\pm 10$ -degree fibers in the crown and keel regions of the shell with overlaps.

Table 2. Measured shell structural performance

	Shell A	Shell B
Prebuckling axial stiffness, lb/in.	531,160	328,690
Global buckling load, lbs	38,810	17,190
Postbuckling load, lbs	17,330	12,560



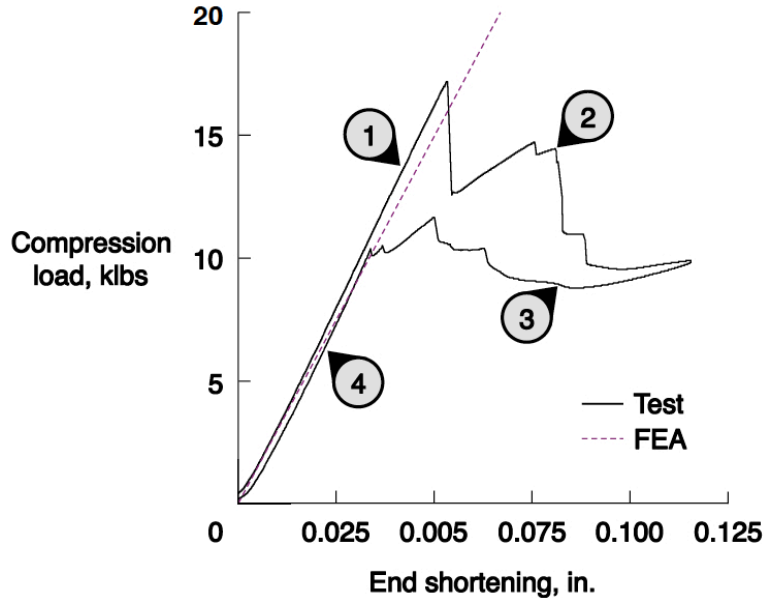


Figure 11. Shell B load-displacement plot

As the axial displacement is increased, this linear prebuckling response is then followed by an unstable dynamic shell buckling event at the junction between Zones 1 and 2, when the shells were observed to buckle at 38.8 and 17.2 klbs for Shells A and B, respectively, listed in Table 2. In each case, shell buckling was accompanied by a single loud noise, characterized as a sharp, high-frequency *crack* sound for Shell A, and a more muted *pop* sound for Shell B. The measured buckling load of Shell A is 126 percent higher than that of Shell B. As the principal difference between the shells is the additional overlaps on the crown and keel of Shell A, this is also the most likely cause of its much higher buckling load. Almost immediately after initial buckling, the axial loads then drop sharply to 17.3 and 12.6 klbs, as listed in Table 2. The observed shell displacements before and after buckling will be discussed below.

The shells' postbuckling responses observed in Zone 2 are highly nonlinear, as the corresponding axial loads may either increase, decrease, or switch despite the monotonically increasing applied end shortenings. For both shells, the end shortening is increased up to approximately two times the value required to induce global buckling (approximately 0.16 and 0.12 inches for Shells A and B, respectively) to thoroughly characterize their postbuckling behavior. After dividing the maximum end shortening by the 35-in. shell length, the corresponding maximum applied axial strains are 0.46 and 0.33 percent, which are both less than the typical 0.50 percent design strain allowable for unidirectional material.

As shown in Figure 10, the axial load for Shell A gradually decreases to about 11.4 klbs, with additional secondary buckling events (accompanied by formation of new buckle patterns, corresponding noises and load drops) also observed during this phase of the test. The structural response for Shell B is shown in Figure 11, and is, by comparison, much more complicated. After the first buckling event, the axial load increases linearly with the applied end shortening up to about 14.7 klbs. At that time, the shell buckles again with a series of rapid changes in the mode shape. After additional end shortening is applied, the load stabilizes at just under 10 klbs.

Zone 3 then involves gradual removal of the applied end shortening, and is again characterized by a highly nonlinear response. As the shells are unloaded, the buckling modes induced during loading all disappear in the reverse order of their appearance. After sufficient end shortening is removed, the shells return nearly to their initial undeformed shapes. Then, in Zone 4, the shells' load-end shortening responses recover elastically back down their initial prebuckling curves, unloading in the opposite direction of their prebuckling responses from Zone 1. Small amounts of hysteresis are observed between the Zone 1 and Zone 4 load-end shortening traces in Figures 10 and 11. These overall structural responses for these tow-steered shells are similar to the results presented in Ref. 10.

This elastic recovery observed in Zones 3 and 4 seems to indicate that the shells may have returned to their pre-test configurations without permanent damage after all of the applied displacements were removed. However, no assessment of the post-test geometry or non-destructive evaluation of the shells has as yet been made to confirm this hypothesis. Also, while no external evidence of material failure has been observed on the shell inner and outer surfaces after testing, further assessments are required to identify any internal damage from the tests.

To provide some additional insight into the veracity of this hypothesis, the Shell A compression test was repeated. The load-end shortening trace for this second test is also plotted in Figure 10 as a red line. Although the second test is not run to as high an applied end shortening as the first test, its prebuckling axial stiffness is within 800 lb/in. (or 0.15 percent) of the first test's stiffness, and its major buckling event occurred within 120 lbs (or 0.31 percent) of the buckling load reported for the first test in Table 2. This high degree of consistency again strongly suggests that the shells did not sustain permanent damage during the original tests.

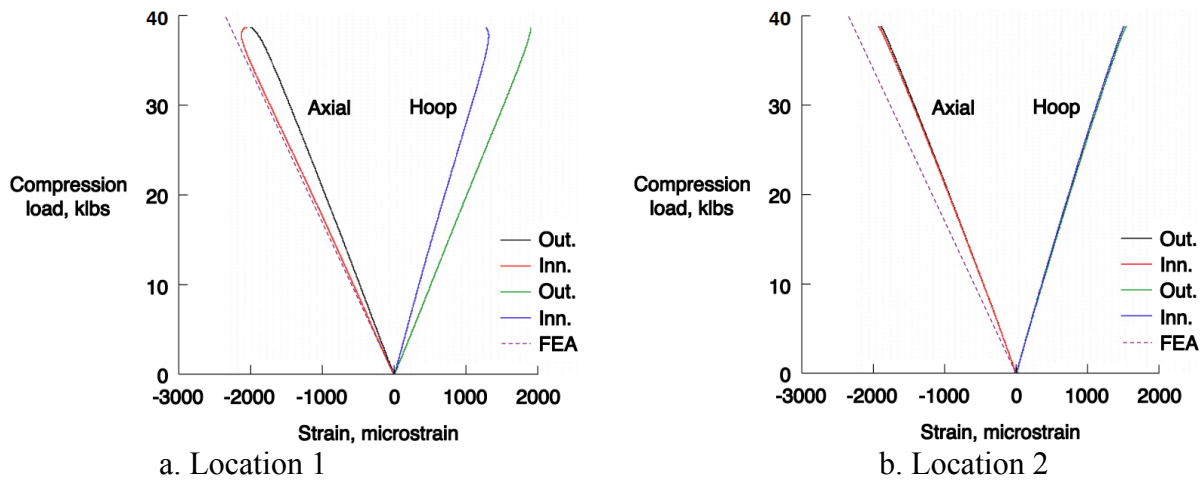


Figure 12. Shell A load-strain plots

#### D. Test results - Strains

Representative measured axial and hoop strains are plotted as functions of the axial load at the tow-steered shell mid-lengths in Figures 12 and 13 for Shells A and B, respectively. These selected strain gage locations on the shell crown, keel and sides are denoted as Locations 1 and 2 (respectively) in Figure 8. These results, plotted only for the prebuckling portion of the shell tests (Zone 1), are generally linear, with some nonlinearity noted either at low load levels or near

global buckling. For clarity, the corresponding shear strains are not reported, as their magnitudes are small, with the vast majority being less than 250 microstrain.

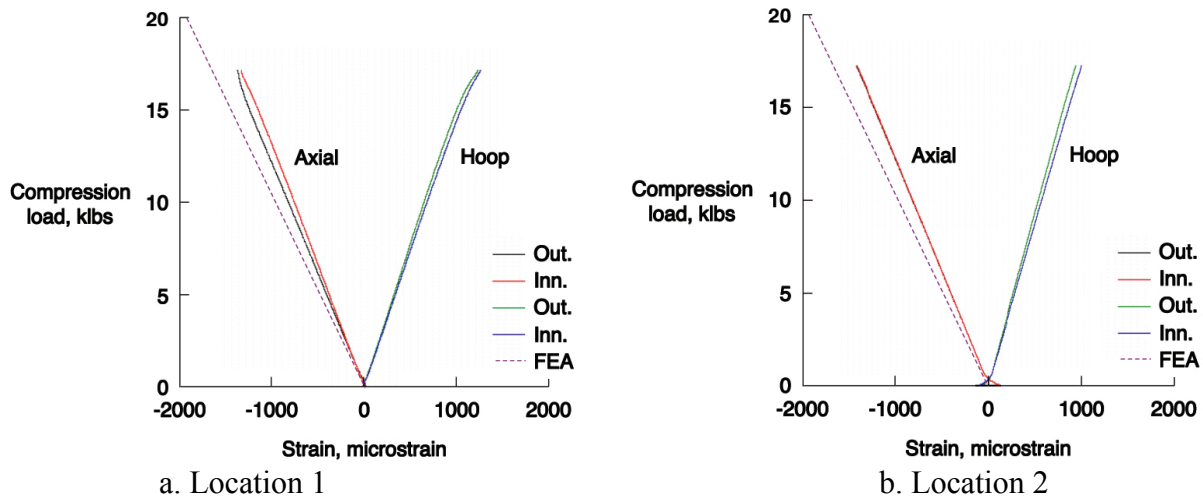


Figure 13. Shell B load-strain plots

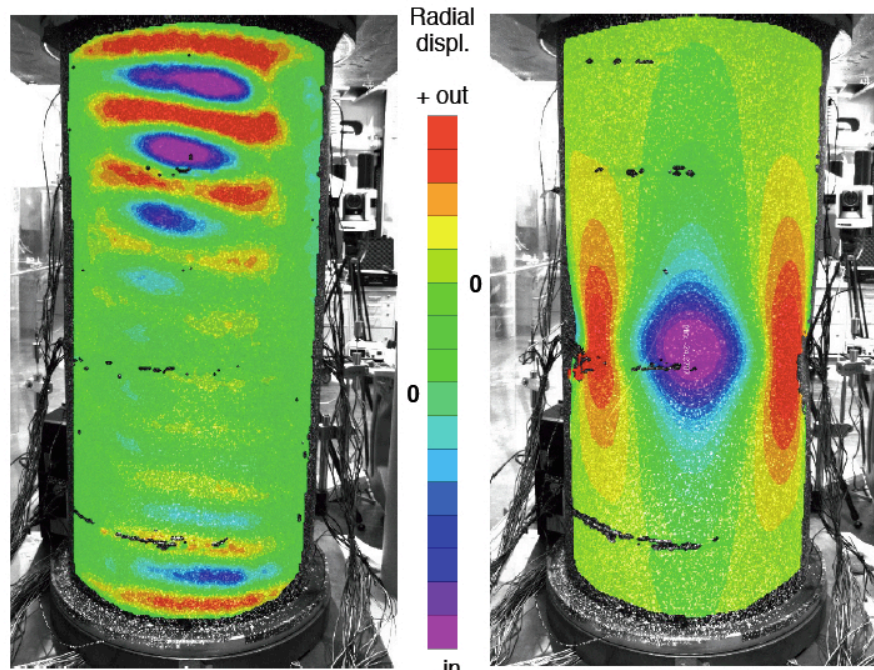
In most cases, the strains measured on the inner and outer surface of the shells are very close to each other. Increasing differences between these back-to-back strains are an indicator of local wall bending, which may be a precursor to either local or global shell buckling. Of the strains presented, the most local bending is observed along the crown of Shell A (Figure 12a), with the initial separation, and then convergence in axial strains, just before buckling, indicating a local reversal in the transverse bending moment. A much smaller amount of local bending is noted at the same location on Shell B in Figure 13a. Almost no local bending is noted in the strain responses plotted for the locations on the sides of both Shells A and B (see Figures 12b and 13b, respectively).

### E. Test results - VIC3D imagery

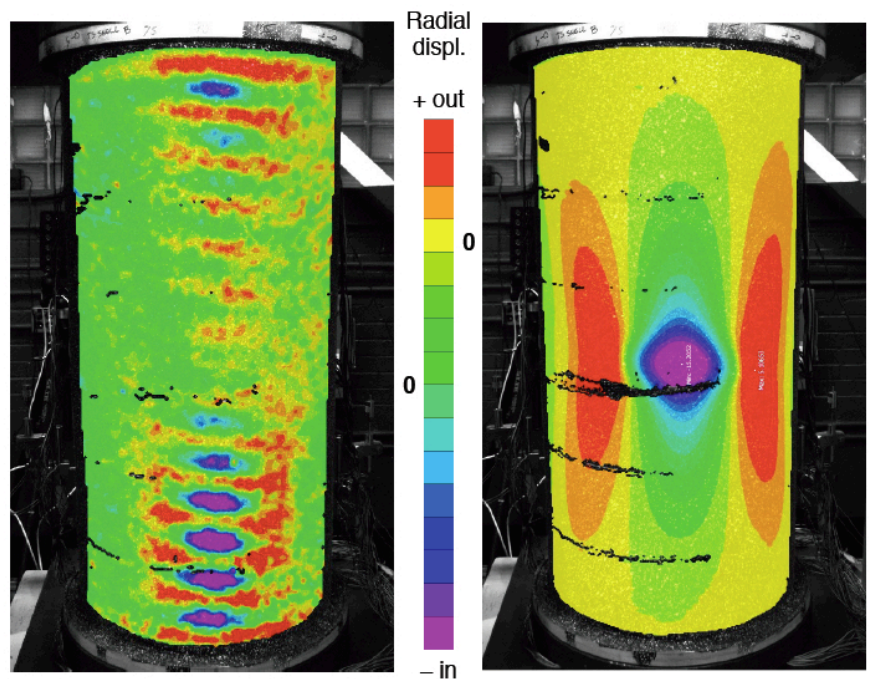
Before buckling, the higher axial stiffnesses of the shells' crown and keel regions generate higher internal force resultants there than in the softer  $\pm 45$  layups on the shell sides. Therefore, the initial buckling instability should occur in the crown and keel regions. Two VIC3D digital image correlation systems are used to provide quantitative full-field imagery (Ref. 11) of the tow-steered shell deformations during the tests. These systems are oriented to view the shell crown and keel during the tests, and to provide high-precision (within  $\pm 0.0015$  in.) visualizations of their displacements. These images are taken at 1-second intervals during the tests.

Representative VIC3D imagery taken during the Shell A compression test are shown in Figure 14. These images show the radial deflections of the back of Shell A just before and after the initial buckling event, at 38.7 and 17.9 klbs, respectively. A qualitative color scale is also shown in the figure, where red indicates the maximum radial deflection outwards from the shell longitudinal axis, and the violet color indicates the minimum radial deflection inwards. The zero value for each image is denoted between the edge of the color scale and the image. The displacement patterns presented here are also replicated on the front of the shell. The radial displacements in the prebuckled image (Figure 14a) show nine full axial sine waves located

along the crown and keel, with the maximum amplitudes of approximately  $\pm 0.01$  in. occurring near the shell ends. These displacements also exhibit a half-sine wave in the circumferential direction.



a. Prebuckling load = 38.7 klbs      b. Postbuckling load = 17.9 klbs  
 Figure 14. Shell A measured radial displacements



a. Prebuckling load = 17.1 klbs      b. Postbuckling load = 12.6 klbs  
 Figure 15. Shell B measured radial displacements

After the shell buckles, the highly loaded crown and keel both rapidly lose their load-carrying capacity, and these loads are then rapidly redistributed to the previously unbuckled regions of the shell. The resulting stable postbuckling displacements shown in Figure 14b show a single inwardly directed diamond-shaped buckle, which is accompanied by oblong regions on either side that bulge slightly outward. Note that these maximum and minimum postbuckled deflections (approximately +0.20 and -0.40 in., respectively) are several orders of magnitude greater than the prebuckled values.

The corresponding VIC3D displacement contours from the Shell B structural test in Figure 15 are qualitatively similar to those described previously for Shell A. The prebuckling image at 17.1 klbs axial load shows approximately 13 full axial sine waves that are distributed along the shell longitudinal axis, with maximum amplitudes of  $\pm 0.004$  in. occurring near the potted shell ends. The postbuckled image is also similar to Shell A, showing maximum and minimum out-of-plane deflections of approximately +0.17 and -0.55 inches, respectively.

#### F. Test results - Platen rotations

In an ideal situation, the loading platens would remain perfectly parallel for the entire duration of the test. However, the physical design of the test machine does allow for some minimal platen rotation to take place under load. Figure 16 shows a plan view sketch of the test machine platen, where the individual LVDT locations at the platen corners are numbered 1 through 4. Positive directions for the platen rotations  $\phi_1$  and  $\phi_2$  are also shown in the figure.

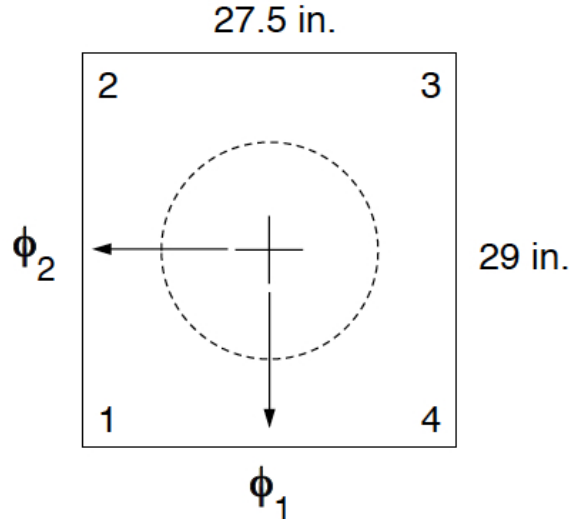


Figure 16. LVDT layout on test machine platen

To compute the relative platen rotations, the two axial displacements along the left edge (LVDTs 1 and 2), right edge (LVDTs 3 and 4), front edge (LVDTs 1 and 4), and back edge (LVDTs 2 and 3) are first averaged. These average values are the axial displacements at the midpoint of each edge, which are then subtracted to determine the differential axial displacements (left minus right, and back minus front) across the platen face. Assuming that the platen rotations are small, their magnitudes are approximated by dividing the differential axial displacements by the corresponding platen dimension.

The platen rotations for the tow-steered shell tests are calculated for the prebuckling phase of the tests (Zone 1). The results for Shell A in Figure 17a show a near-linear increase in both rotation angles with increasing load, up to a maximum value of approximately 0.01 degrees. The corresponding rotations for Shell B are plotted in Figure 17b. The maximum rotation  $\phi_1$  about that shell's crown-keel axis is comparable to those of Shell A. However, the rotation  $\phi_2$  about the shell side-to-side axis is much smaller, with a magnitude of approximately 0.0025 degrees outside the initial nonlinearity at low loads. These results, while small, indicate that unanticipated bending moments are applied to the shells during the tests, and may need to be modeled to fully correlate the test results with the analyses.

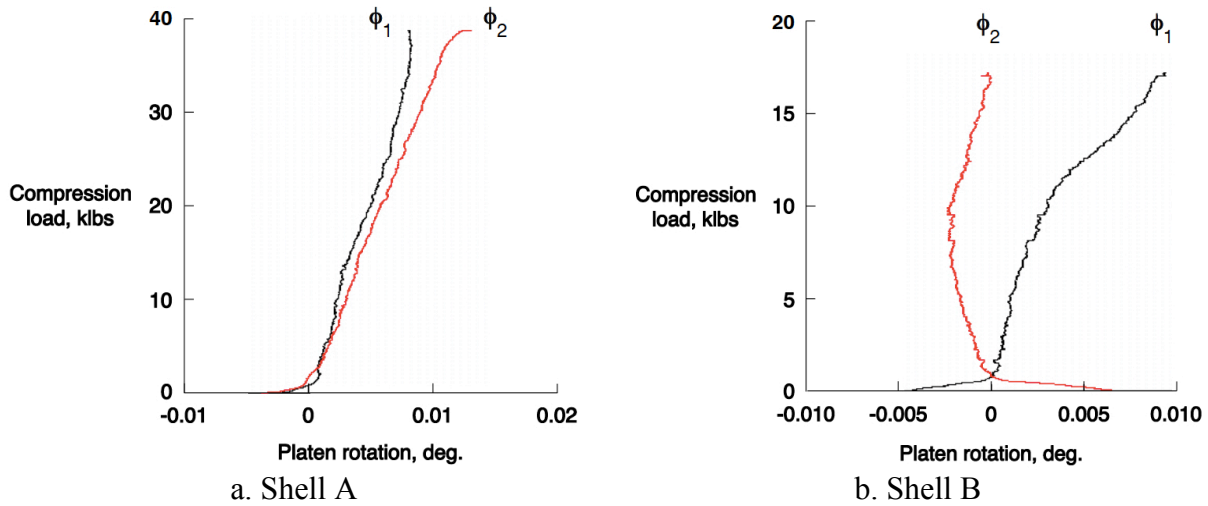


Figure 17. Measured platen rotations

## V. Preliminary shell finite element analyses

Finite element models of the two composite tow-steered shells are developed using NASTRAN (Ref. 12). These models are used to perform linear static and bifurcation buckling analyses to provide estimates of the shells' structural responses prior to conducting the compression tests. These analysis results are also used after testing to provide preliminary comparisons with the measured data prior to performing more detailed structural analyses that may include geometric and material nonlinearities (Ref. 13). The analysis models developed for this study and the results generated are described and discussed in this section.

### A. Model description

A converged finite element model of the tow-steered shells is developed with 204 elements in the circumferential direction and 140 elements in the axial direction. Linear quadrilateral CQUAD4 shell elements are used for these analyses. The shell geometry is first idealized as a right circular cylinder, and measured radial imperfections (which are measured after the shell is removed from the mandrel, but before the potting is applied to the shell ends; Ref. 4) are then mapped onto the finite element mesh to determine their effect on the shell structural response. The measured IM7/8552 material properties listed in Table 1 are used for both finite element models. However, a uniform ply thickness of 0.0050 in./ply is used for these analyses, which is 7.4 percent thinner than the average ply thickness measured directly from the material test

coupons. This reduced ply thickness is selected to be consistent with the average wall thicknesses measured for these shells in Ref. 4.

To compute the shell structural response, the nodes on both ends of the shell model are clamped, except for one end where the axial displacements are unconstrained. At that end, a “wagon-wheel” of rigid elements (RBE2) connects the top perimeter of nodes in the shell to a central node where the compressive axial force is applied. This modeling approach closely replicates the uniform end shortening that is applied to the shell using the test machine. The lateral constraint of the potted shell ends is then modeled by assuming that the lateral deflections of the nodes within the potting are zero.

One of the many challenges in the modeling and analyses of tow-steered structures is how best to represent the continuous variation of the laminate thicknesses and fiber orientation angles when using discrete techniques like the finite element method. For these analyses, the laminate thickness and layup (ply fiber orientation angles) are both assumed to be constant within each finite element. Due to different degrees of symmetry within the laminate stacking sequences, the finite element model for Shell A requires 174 different PCOMP cards distributed over the 28,560 CQUAD4 elements, while the analysis model for Shell B requires only 51 unique PCOMP cards. The effects of radial offsets for each individual element (due to the fact that the shell is built on a smooth cylindrical mandrel, and all overlaps are displaced radially outward) are also evaluated using the NASTRAN model.

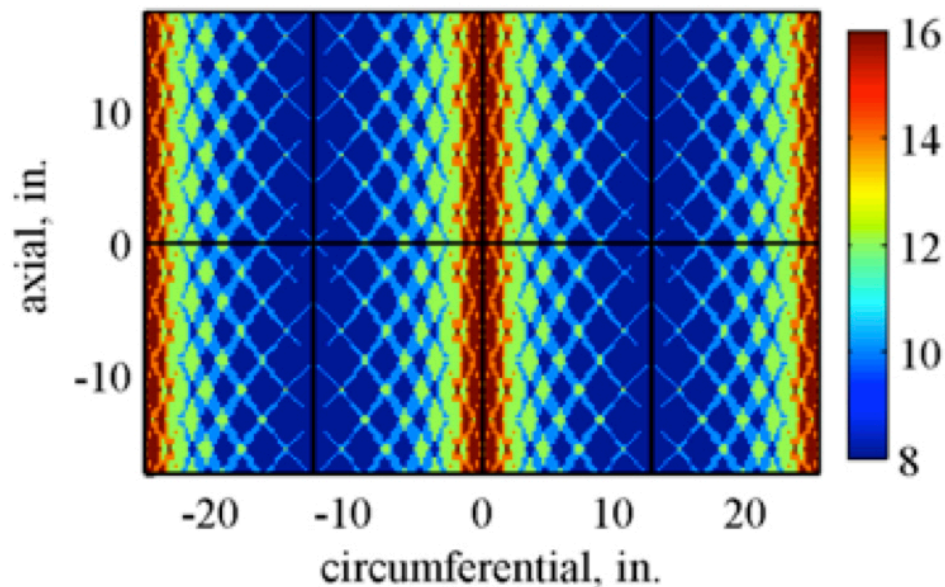


Figure 18. Shell A finite element model laminate thicknesses

For the preliminary analyses presented here, the courses and fiber angles are obtained in an idealized fashion, as described in Ref. 3. In this approach, the courses are defined as circular arcs, and the angles are a function of the element centroid’s circumferential location. The modeled laminate thicknesses for the Shell A finite element model, shown in Figure 18, agree well with the predicted shell thicknesses in Figure 3. While the data plotted in Figure 3 show a small number of locations with 18 plies, the finite element model has a maximum of 16 plies

around the crown and keel. When the tow drops shown in Figure 4 are not modeled, the resulting idealized laminate thicknesses for Shell B are all equal to 8 plies. The ply 3 fiber orientation angles in Figure 19 are also comparable to those shown in Figure 4, although their idealized nature is also highlighted by the lack of tow drops, which may result in a higher local stiffness and stress state in the analysis model.

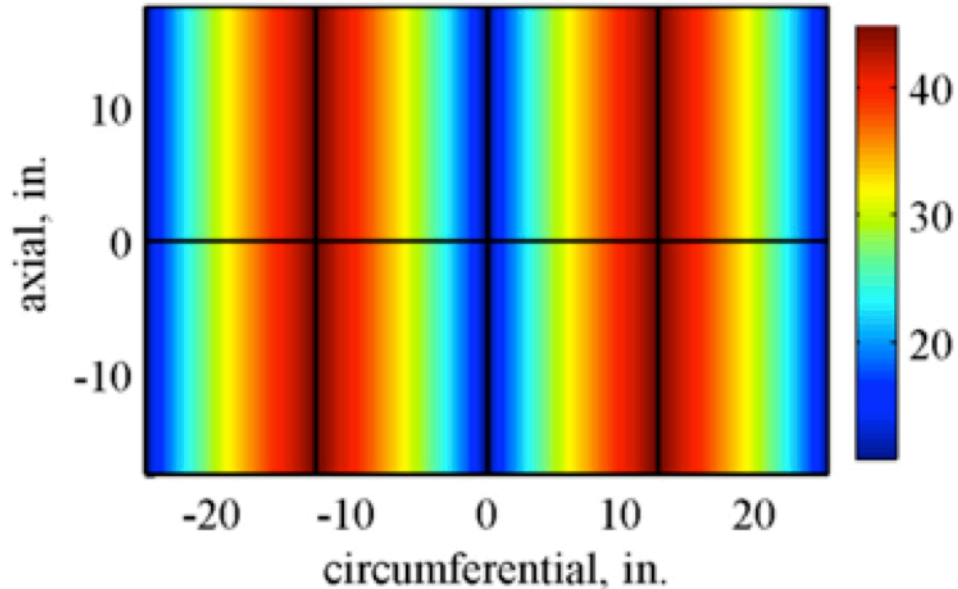


Figure 19. Shell A and B finite element model ply 3 fiber orientation angles

## B. Preliminary analysis results

These NASTRAN finite element models are then used to perform linear structural analyses of the tow-steered shells. The prebuckling axial stiffness of each shell is calculated from a static analysis by dividing the force applied to the central node of the wagon wheel of RBE2 elements by the uniform axial deflection at that loaded end of the shell. Results from these analyses are reported in Table 3, and show that the prebuckling axial stiffness for Shell A is 63 percent greater than that of Shell B.

Table 3. Predicted shell structural performance

	<b>Shell A</b>	<b>Shell B</b>
Prebuckling axial stiffness, lb/in.	486,111	298,337
Buckling load (no imperfs.), lbs	35,813	15,054
Buckling load (with imperfs.), lbs	36,005	14,761

Linear bifurcation buckling loads from eigenanalyses of the tow-steered shells without geometric imperfections or laminate offsets are also listed in Table 3. The predicted buckling load for Shell A is 138 percent greater than the corresponding value for Shell B. The predicted buckling mode shape for Shell A, shown in Figure 20, has nine sinusoidal waves (oriented along the axial direction) localized to the stiffer  $[\pm 45/\pm 10]_s$  regions along the shell crown and keel, which act as large axial stiffeners and carry much higher axial loads than the softer  $[\pm 45]_{2s}$  sides. The



maximum amplitudes occur near the shell middle. There is a slight axial asymmetry of the deflections between the shell top and the bottom, and these buckled lobes are oriented at a slight angle. The linear buckling mode shape for Shell B is shown in Figure 21. This mode shape is somewhat similar to the mode shape for Shell A, although the axial wavelength of each buckled lobe is smaller (i.e., more waves), with 12 full sine waves along the shell length.

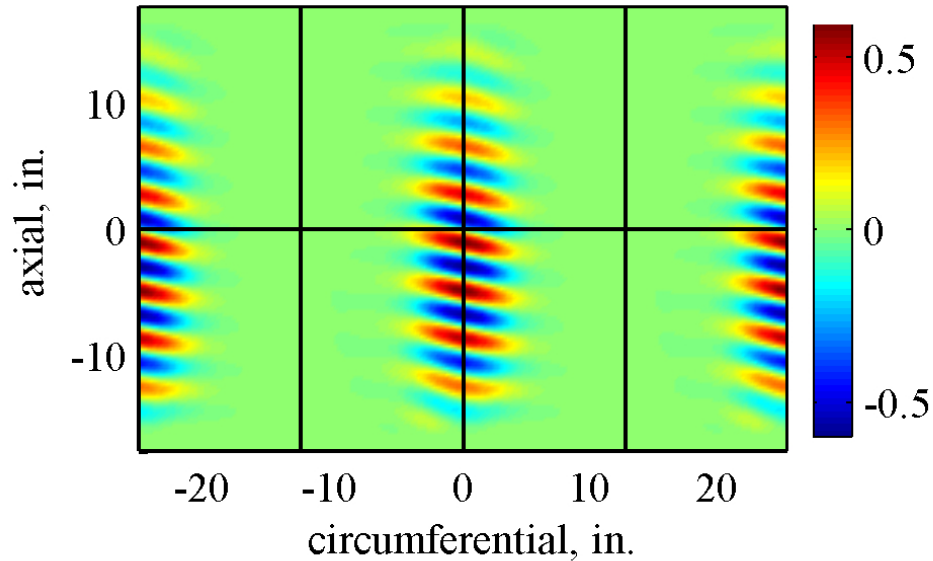


Figure 20. Shell A without imperfections predicted buckling mode shape

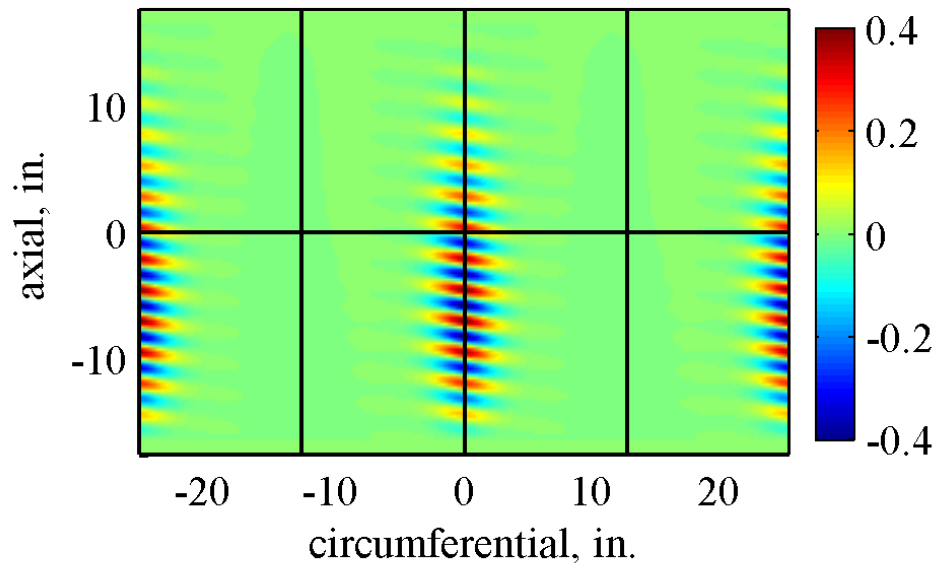


Figure 21. Shell B without imperfections predicted buckling mode shape

To explore the effect of the geometric imperfections on shell performance, the measured imperfection data (shown in Figure 22) from Ref. 4 are mapped onto the finite element model meshes. When the buckling eigenanalyses are repeated with the imperfections, the predicted loads do not change significantly. However, the single symmetric mode shape observed previously for the analyses without imperfections (see Figures 20 and 21) now separates into two

closely spaced modes for the cases with imperfections. For Shell A, the predicted buckling load actually increases by about 0.5 percent, with the first buckling mode having all of its lobes located along the shell keel, and the second mode with its lobes located along the crown. This result is perhaps atypical in that the inclusion of imperfections will typically result in a reduction in buckling load. The corresponding results for Shell B show a reduction in critical load of about 2 percent for the case with imperfections, with a similar separation of the buckling modes. The predicted buckling loads for both shells with imperfections are also listed in Table 3. Furthermore, inclusion of the laminate offsets also has a minimal effect, with the buckling loads of Shell A increasing by less than 1 percent for both cases with and without the geometric imperfections.

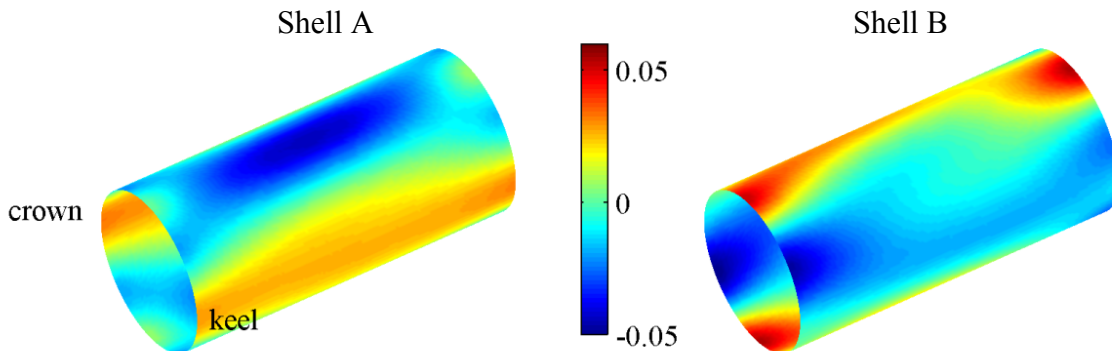


Figure 22: Measured geometric imperfections, in. (Ref. 4)

## VI. Discussion of test and analysis results

The test results and preliminary finite element analyses are compared in this section. The predicted shell prebuckling axial stiffnesses for Shells A and B from Table 3 are plotted on the load-end shortening curves in Figures 10 and 11, respectively. The predicted shell axial stiffnesses, shown as dashed lines in the figures, are 8.5 and 9.2 percent lower, respectively, than their corresponding measured values. The predicted buckling loads for Shells A and B reported in Table 3 are 7.7 and 12.4 percent lower (respectively) than the experimental buckling loads from Table 2. While the preliminary analysis results presented in Table 3 compare relatively well with the measured shell performance shown in Table 2, more detailed finite element analyses should help to provide additional insight into the reasons for these differences.

To estimate the predicted prebuckling strains, the prebuckling axial stiffness values in Table 3 are multiplied by the overall shell length of 35 inches to determine the shells' adjusted axial stiffnesses. These resulting values (17014 klbs for Shell A, and 10442 klbs for Shell B) are then superposed as dashed lines on the corresponding measured load-axial strain responses in Figures 12 and 13, respectively. When compared with the slopes of the measured average axial strains in the figures, these predicted adjusted axial stiffnesses are consistently lower, and range from 10.5 to 17.6 percent below the test results.

A qualitative comparison of the measured (Figures 14a and 15a) radial deformations with the predicted buckling mode shapes (Figures 20 and 21) is interesting. While both sets of deformed shapes show almost identical numbers of sinusoidal waves along the shell lengths and circumferentially, the maximum amplitudes occur in completely different locations. Whereas

the measured maximum amplitudes are located at the top and bottom of the shells, the predicted maximum amplitudes occur at the shell middle. In addition, the analytical mode shapes are much more compact, while the experimental results appear to be more widely distributed along the shell length. Additional nonlinear finite element analyses must be performed to better understand these differences.

## VII. Concluding remarks

Two advanced composite tow-steered shells, manufactured using a fiber placement system, are tested in end compression and analyzed using linear finite element analyses. Both shells have the same circumferential variation in fiber orientation angles, which vary continuously from  $\pm 10$  degrees on the shell crown and keel, to  $\pm 45$  degrees on the shell sides. The shells differ in that Shell A has the full 24-tow band width applied during each course (resulting in local ply overlaps and thickness variations), while Shell B uses the tow drop/add capability of the fiber placement system to maintain a more uniform shell wall thickness. In general, the test and analysis results compare well, with prebuckling axial stiffnesses and buckling loads agreeing within an average of 10 percent.

Shell A has a measured prebuckling axial stiffness that is 62 percent higher than that of Shell B, and a measured buckling load that is 126 percent higher than that of Shell B. When adjusted by their corresponding shell weights (Shell A is 27 percent heavier than Shell B), Shell A has a normalized prebuckling stiffness that is 28 percent higher than that of Shell B, and a normalized buckling load that is 78 percent higher than that of Shell B. These results show that significant gains in structural performance may be achieved (in this case through the axially stiff overlaps) by judicious placement of the load-bearing material within the structure.

Both isotropic and uniformly laminated (i.e., the same stacking sequence at every point) cylinders have been shown to be highly sensitive to imperfections. However, the tow-steered cylinders studied do not appear to exhibit the same high degree of sensitivity. Therefore, a reasonable assumption is that the non-uniform stiffness distribution in these cylinders is the cause, although additional research is required to identify the exact reason. Preliminary comparisons between linear bifurcation buckling loads and nonlinear limit point buckling loads also show minor differences, which further supports an insensitivity to imperfections.

Higher-fidelity structural analyses must also be performed to better correlate with the observed test data. Specifically, a nonlinear buckling analysis and investigation of the post-buckled load-displacement regions may be warranted. These analyses could also include the effects of the bending moments induced during test from the platen rotations, the as-manufactured fiber angles and laminate thickness variations generated from shell manufacturing data, the effects of geometric and material nonlinearities, and progressive damage modeling.

## References

1. Z. Gürdal, B. F. Tatting and K. C. Wu: *Variable Stiffness Composite Panels: Effects of Stiffness Variation on the In-Plane and Buckling Response*. Composites Part A: Applied Science and Manufacturing, Vol. 39, No. 5, 2008. Pages 911-922.

2. D. O. Evans: *Fiber Placement*. Handbook of Composites, 2nd edition, S. T. Peters, editor. Chapman & Hall, London, 1998. Pages 476-487.
3. K. C. Wu: *Design and Analysis of Tow-Steered Composite Shells Using Fiber Placement*. Proceedings of the ASC 23rd Annual Technical Conference. Memphis, Tennessee, September 9-11, 2008. Paper no. 125.
4. K. C. Wu, B. F. Tatting, B. H. Smith, R. S. Stevens, G. P. Occhipinti, J. B. Swift, D. C. Achary and R. P. Thornburgh: *Design and Manufacturing of Tow-Steered Composite Shells Using Fiber Placement*. Proceedings of the 50th AIAA/ASME/ASCE/AHS/ASC Structures, Structural Dynamics and Materials Conference. Palm Springs, California, May 4-7, 2009. Paper no. AIAA 2009-2700.
5. A. Blom, M. Rassaian, P. B. Stickler and Z. Gürdal: *Modal Testing of a Composite Cylinder with Circumferentially Varying Stiffness*. Proceedings of the 50th AIAA/ASME/ASCE/AHS/ASC Structures, Structural Dynamics and Materials Conference. Palm Springs, California, May 4-7, 2009. Paper no. AIAA 2009-2558.
6. A. Blom, P. B. Stickler, M. Rassaian and Z. Gürdal: *Bending Test of a Variable-Stiffness Fiber Reinforced Composite Cylinder*. Proceedings of the 51st AIAA/ASME/ASCE/AHS/ASC Structures, Structural Dynamics, and Materials Conference. Orlando, Florida, 12-15 April 2010, Paper AIAA-2010-2600.
7. A. B. Hulcher, D. M. McGowan, B. W. Grimsley, N. J. Johnston and G. H. Gordon: *Processing and Testing of Thermoplastic Composite Cylindrical Shells Fabricated by Automated Fiber Placement*. Proceedings of the 47th International SAMPE Symposium. Long Beach, California, 12-16 May 2002. Pages 1812-1826.
8. K. Martlett: *Hexcel 8552 IM7 Unidirectional Prepreg 190 gsm & 35%RC Qualification Material Property Data Report*. National Center for Advanced Materials Performance, Wichita, Kansas. Test Report CAM-RP-2009-015, Rev. A, April 22, 2011.
9. Anon.: *Standard Test Method for Compressive Properties of Rigid Plastics*. ASTM D695-10, ASTM International, West Conshohocken, PA, 2010.
10. C. Hühne, R. Rolfes, E. Breitbach and J. Teßmer: *Robust Design of Composite Cylindrical Shells Under Axial Compression—Simulation and Validation*. Thin Wall Structures (46) 2008. Pages 947–962.
11. M. A. Sutton, J. J. Orteu and H. Schreier: *Image Correlation for Shape, Motion and Deformation Measurements: Basic Concepts, Theory and Applications*. Springer, New York 2009.
12. Anon.: *MSC Nastran 2012 Quick Reference Guide*. MSC Software Corporation, Santa Ana, California, 2011.
13. M. W. Hilburger and J. H. Starnes: *High-Fidelity Nonlinear Analysis of Compression-Loaded Composite Shells*. Proceedings of the 42nd AIAA/ASME/ASCE/AHS/ASC Structures, Structural Dynamics and Materials Conference. Seattle, Washington, 16-19 April, 2001. Paper no. AIAA 2001-1394.